Dynamics of a dense laboratory plasma jet investigated using soft x-ray laser interferometry

Jonathan Grava,[1] Michael A. Purvis,[1] Jorge Filevich,[1] Mario C. Marconi,[1] Jorge J. Rocca,[1,2] James Dunn,[3] Stephen J. Moon,[3] and Vyacheslav N. Shlyaptsev[4]

[1]*NSF ERC for Extreme Ultraviolet Science and Technology, and Department of Electrical and Computer Engineering, Colorado State University, Fort Collins, Colorado 80523, USA*

[2]*Department of Physics, Colorado State University, Fort Collins, Colorado 80523, USA*

[3]*Lawrence Livermore National Laboratory, Livermore, California 94551, USA*

[4]*Department of Applied Science, University of California–Davis, Livermore, California 94551, USA*

(Received 2 April 2008; published 17 July 2008)

The formation and evolution of a collisional aluminum plasma jet created by optical laser irradiation of triangular grooves with pulses of 120 ps duration at an intensity of 1×10^{12} W cm^{-2} were studied with experiments and simulations. Series of high-contrast soft x-ray laser interferograms obtained with a 46.9 nm laser mapped the plasma density evolution of an initially narrow plasma jet that expands along the symmetry plane and evolves into a broader plasma plume with significant side lobes. Two-dimensional simulations performed using the radiation hydrodynamic code HYDRA reveal that the jet formation is initiated by accelerated material ablated from the vertex and is augmented by the continual sequential arrival of wall material along the symmetry plane, where it collides and is redirected outward. Radiative cooling is identified as an important process in maintaining the collimation of the jet. These results demonstrate that well collimated collisional plasma jets with parameters in a range of interest can be generated with low-energy laser pulses (<1 J), opening the possibility of studying relevant plasma phenomena in a small laboratory setting.

DOI: 10.1103/PhysRevE.78.016403 PACS number(s): 52.70.−m, 95.75.Kk, 52.65.−y

I. INTRODUCTION

Understanding the formation and evolution of plasma jets is of significant interest in various fields. In the astrophysical context, highly collimated jets are observed to originate from active nuclei galaxies [1] and young stellar objects [2], with parameters that cover many orders of magnitude in velocity and spatial extent. Numerous observations have been reported [3,4] and their dynamics have been modeled with numerical simulations [5,6]. Laboratory experiments can produce small-scale plasma jets and shocks [7–13], some of which are relevant to astrophysics [14–17]. These experiments also give insight into jets and shock physics. For example, unwanted shock waves through inertial confinement fusion capsule defects can produce jets of material that mix ablator with fuel, resulting in a reduced yield [7,11,12].

Numerical models of plasma jets are complex codes that take into account hydrodynamic and atomic processes, including the transport of radiation. In order to validate the models, experiments can be designed to create plasma jets with different characteristics, including scaled versions of astrophysical jets [18]. High Mach number jets were experimentally produced and studied using *Z*-pinch arrays [19]. Highly radiative jets have also been created using high energy ($\sim$0.1–1 kJ) laser pulses from large lasers such as the Nova [15], Gekko XII [17], Omega [7], and PALS Asterix [9,10] to irradiate conical and flat targets. Plasma jets have also been produced by irradiation of different target geometries using smaller lasers ($\sim$10–15 J) [13,20]. While imaging, spectroscopy, and other techniques have been used to study the behavior of plasma jets [7,13,17], accurate two-dimensional maps of the electron density can only be directly obtained with interferometry. Interferometry with visible and ultraviolet light has been extensively used to study a wide variety of plasmas [21]. However, the use of optical interferometry is limited by the strong refraction caused by large density gradients. Also limiting is the increased number of fringe shifts resulting from large plasma densities and size, which cannot be resolved. It is possible to overcome these limitations with the use of short-wavelength laser probes. Soft x-ray light can propagate through plasmas that have steeper density gradients and larger size, with significantly reduced refraction and with a smaller number of fringe shifts, permitting the measurement of higher densities. This has motivated the development of soft x-ray laser interferometry as a tool to probe dense plasmas [22–32]. In particular, Wan *et al.* used a 15.5-nm-wavelength soft x-ray laser probe to obtain interferograms of plasmas created by focusing the fusion-class laser NOVA at an intensity of 3×10^{14} W cm^{-2} onto two Au slab targets placed at 45 degree with respect to the symmetry plane [23]. Plasma density profiles were measured to reach an electron density of 6×10^{20} cm^{-3} on axis. Hydrodynamic simulations using the code LASNEX predicted a stagnation width similar to that observed in the experiment. However, the code predicted the appearance of an off-axis electron density peak as soon as the plasma started to collide, a feature that was not observed experimentally. In this paper, we present the study of a dense hydrodynamic plasma jet created by irradiation of a triangular V-shaped cavity with low-energy laser pulses (<1 J). The formation and evolution of the jet was studied combining soft x-ray laser interferometry and emission spectroscopy with two-dimensional (2D) hydrodynamic simulations. The target geometry differs from that investigated by Wan *et al.* in that the wall of the cavity wall is continuous, without an opening at the vertex. The plasma originating from the vertex was found to initiate the formation of a thin and long plasma sheet that is augmented by the convergence of wall plasma on the symmetry plane of the target, where it is redirected outward.

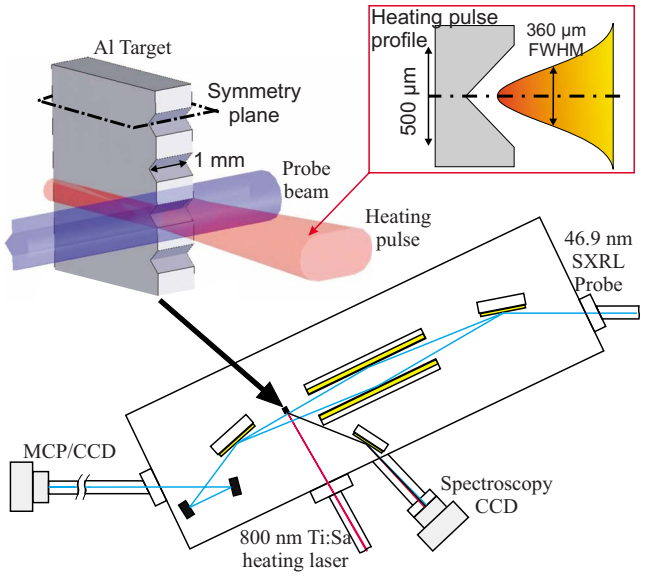

FIG. 1. (Color online) Schematic representation of the plasma interferometry setup. The top left inset shows a V-shaped grooved target. The heating beam (in red) deposits the energy at the bottom of the cavity and the soft x-ray (SXR) probe beam (in blue) travels through the 1-mm-long plasma. The inset in the top right represents the profile of the 350 μm FWHM heating beam.

The next section describes the setup used in the experiments, and Sec. III presents the experimental results. These results are discussed in combination with hydrodynamic simulations in Sec. IV.

II. EXPERIMENTAL SETUP

The triangular cross-section targets used to create the plasma are schematically represented in the top-left insert of Fig. 1. A set of 90 degree angle triangular grooves was machined in a 1-mm-thick strip of aluminum. The 1-mm-long grooves are 250 μm deep and their width at the target surface is 500 μm. The plasma was created by irradiating an individual groove with a 0.8 J laser pulse of 120 ps duration produced by a $\lambda=800$ nm Ti: sapphire laser. The laser beam was shaped into a 1.5-mm-long line focus of 360 μm width with an intensity of $\sim 1\times 10^{12}$ W cm^{-2}. The laser pulse was measured to be free of any significant prepulses. A reference interferogram without plasma present and up to two plasma interferograms with good reproducibility were taken for each groove before moving the target to another groove. The line focus energy distribution and position on the target were monitored for consistency and recorded on every shot. The good shot-to-shot reproducibility allowed the mapping of the evolution of the plasma with the 30-40 interferograms that were obtained with a single target strip.

The interferograms were obtained using a setup composed of an amplitude division soft x-ray interferometer [26] and a 46.9 nm tabletop soft x-ray capillary discharge laser probe [33] schematically represented in Fig. 1. The Ne-like Ar capillary discharge laser emits pulses of $\sim$1.2 ns duration and $\sim$0.15 mJ of energy. The good spatial coherence of the laser simplifies the task of generating interferograms with high fringe visibility [34]. The inherent jitter of the discharge was reduced to $\sim$2 ns by laser triggering the spark-gap switch that controls the firing of the capillary discharge, enabling the acquisition of "snapshots" of the plasma at selected times during its evolution. The interferometer is based on a skewed Mach-Zehnder configuration where two diffraction gratings are used to split and recombine the beams. The blaze angle of the gratings was chosen to generate zero- and first-order diffracted beams of similar intensity when the incident angle is 11 degrees. Two long gold-coated mirrors are positioned at a grazing incidence angle of 2.6 degrees to redirect the beams toward the second grating, which recombines the beams to generate the interference pattern. The plasma was imaged with 25$\times$ magnification using a Sc/Si multilayer-coated spherical mirror with $\sim$40% reflectivity onto a multichannel plate/phosphorus screen detector read by a CCD camera [35]. The target, which was mounted on a motorized *XYZ* stage to allow precise alignment under vacuum, was placed intercepting the zero-order path of the interferometer between the folding mirror and the second grating. Two fast photodiodes were used to record the time of arrival of the soft x-ray probe pulse with respect to the Ti: sapphire heating pulse. The time delay between the peaks of each of the two signals was measured with an error of $\sim$200 ps. A more complete description of the soft x-ray interferometer and its alignment procedure can be found in a previous publication [26].

Time-integrated spectra of the soft x-ray plasma emission were obtained using a variable-space grating that is aberration-corrected for operation at a grazing incidence angle of 3 degrees [36]. The spectra were recorded using a back-illuminated 1024×1024 pixels charge-coupled device (CCD) camera, positioned to collect light in the 35–185 Å wavelength range. A 200-nm-thick Zr filter was used to block visible light.

III. EXPERIMENTAL RESULTS

A time-integrated image of the plasma self-emission at wavelengths $\lambda<1000$ Å is shown in Fig. 2. The irradiating laser beam is incident on the target from the right. Most of the emission originates from a thin (50-μm-wide) elongated plasma sheet (1 mm long) localized along the symmetry plane of the groove. Weaker emission is also observed from plasma near the wall.

A sequence of interferograms that maps the evolution of these aluminum plasmas is shown in Fig. 3. The timing of each image is measured with respect to the arrival of the 120 ps heating pulse. The white lines outline the original position of the target, obtained for each shot from a preceding reference interferogram without the plasma present. Electron density maps were calculated from the interferograms by assuming that the 1 mm plasma is uniform along the propagation direction of the probe beam. The plasma is initially uniform in this direction because the 1.5 mm full width at half-maximum (FWHM) plasma heating beam overfills the 1-mm-long target. However, while the pressure gradients cause the plasma to expand mainly in the direction perpendicular to the walls, lateral expansion could degrade the axial

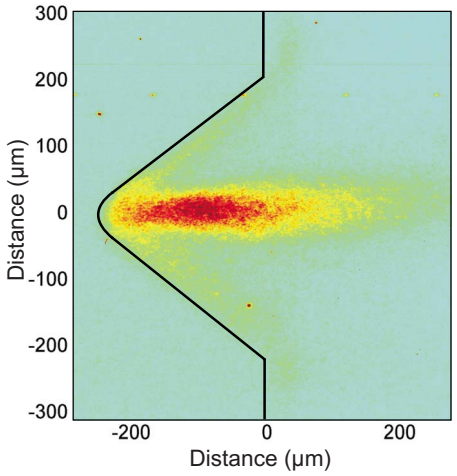

FIG. 2. (Color online) Time-integrated emission of the laser-created aluminum plasma jet.

uniformity. To evaluate this effect, shots with identical irradiation intensities were obtained for targets of two different lengths: 1 and 0.5 mm. Analysis of the interferograms for these two target lengths found that the densities differed by ~10%, a variation that is within the measured shot-to-shot variation of the experiment. This observation justifies neglecting plasma edge effects to assume plasma uniformity along the direction of propagation of the probe beam. The number of fringe shifts is in this case directly proportional to the electron density, with $N_{\text{fringe}}=(L/\lambda)(n_e/2n_c)$ for $n_e \ll n_c$, where n_c is the critical density (5×10^{23} cm^{-3} at 46.9 nm) and L is the length of the plasma (1 mm). One fringe shift at this probe wavelength corresponds to a density of 5×10^{19} cm^{-3}. Therefore, a map of the electron density can be constructed by measuring the number of fringe shifts with respect to a reference interferogram obtained without plasma present. The error in determining the number of fringe shifts is estimated to be ~1/10th of a fringe shift, which amounts to an uncertainty of 5×10^{18} cm^{-3} in the density values. Additional uncertainty of similar magnitude results from shot-to-shot variations and the lateral expansion discussed above. The aforementioned analysis of the interferograms also assumes that the plasma index of refraction is dominated by the contribution from free electrons. This is not always the case at soft x-ray wavelengths, as bound electrons can significantly contribute to the index of refraction [37]. However, calculations showed that in the case of aluminum plasmas, the contribution of bound electrons to the index of refraction can be neglected at the 46.9 nm probe wavelength.

Figure 4 shows the electron density maps corresponding to the interferograms of Fig. 3. The 1.1 ns frame shows the formation of a narrow (~30-μm-wide) plasma jet with a large length-to-width ratio, ~10:1 along the symmetry plane of the groove. The jet was measured to initially expand at a velocity of $\sim(3\pm1)\times10^7$ cm s^{-1} along the symmetry plane. At this time the interference fringes within the region of the jet are not completely resolved due to a combination of refraction of the probe beam by steep density gradients and motion blurring. The subsequent frame at 2.6 ns shows that the plasma continues to expand rapidly along the symmetry

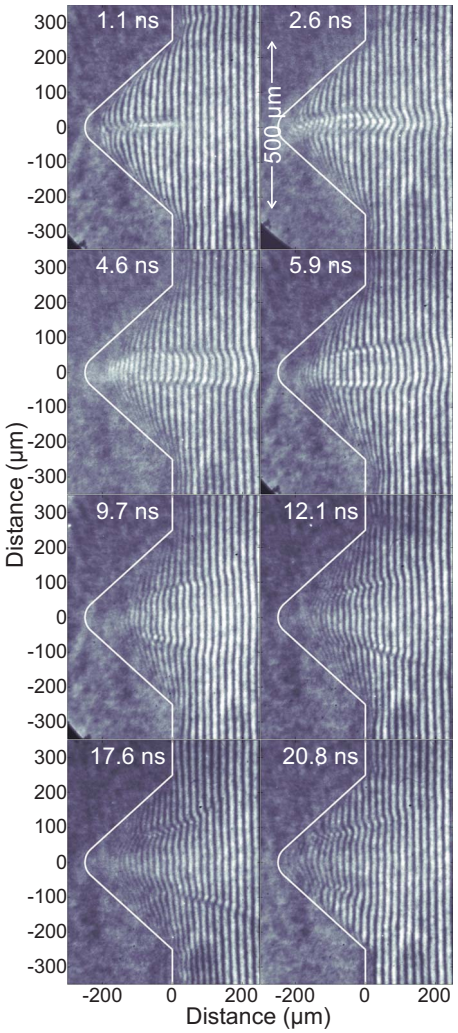

FIG. 3. (Color online) Sequence of soft x-ray interferograms mapping the evolution of laser-created aluminum plasma. The white solid line represents the original position of the V-shaped groove. The timing is measured with respect to the peak of the heating pulse.

plane, reaching a length of ~530 μm while simultaneously broadening to a plume ~80 μm wide. At this time, the highest electron density measured along the symmetry plane reaches 1.2×10^{20} cm^{-3} at ~100 μm away from the bottom of the cavity. At later times, the central plasma continues to expand along the symmetry plane, while simultaneously widening to reach a width of ~200 μm, 9.7 ns after the irradiation pulse. The 9.7 ns density map and the subsequent frames show the formation of two dense side lobes that evolve moving slowly away from the symmetry plane of the groove toward the target walls. At these late times, the regions close to the target surface present strong absorption, caused by the presence of a large density of low charge ions that can be photoionized by the 26.5 eV photons of the probe beam. In summary, during the first nanosecond of the evolution, a dense thin elongated jetlike plasma sheet is observed on axis. This jet extends quickly along the symmetry plane. Later in time, the jet widens into a plume that then splits into two distinct side lobes, progressively evolving toward the target walls.

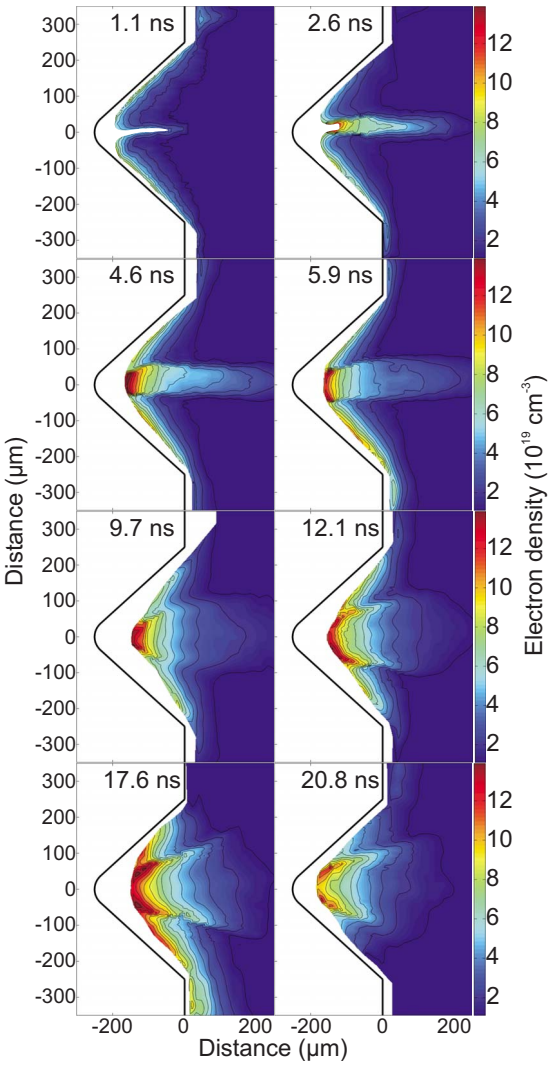

FIG. 4. (Color online) Electron density maps corresponding to the interferograms of Fig. 3. The black solid line outlines the position of the groove. The white regions are locations where the plasma density could not be determined either due to fast plasma motion resulting in blurred fringes (near the symmetry axis), or due to strong absorption of the soft x-ray probe beam by cold plasma (near the walls).

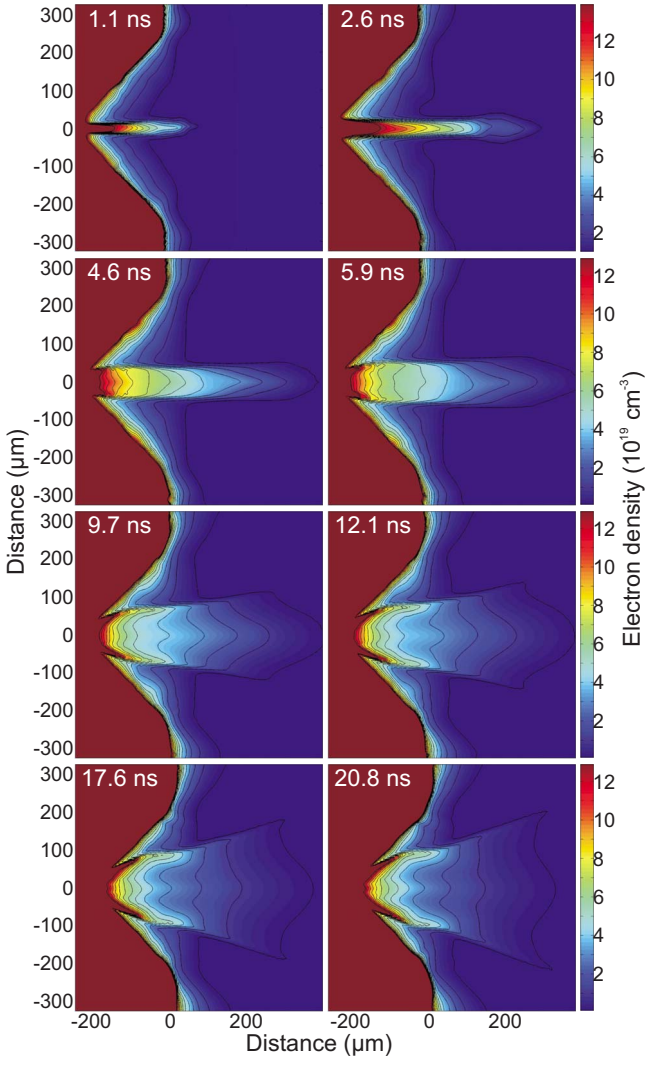

FIG. 5. (Color online) Simulated electron density maps obtained with HYDRA. The code shows good agreement with the measurements in the general behavior of the plasma and maximum electron densities.

IV. SIMULATIONS AND DISCUSSION

In order to help understand the jet formation and subsequent plasma evolution as well as test the ability to accurately simulate the plasma, 2D computations were performed using the single fluid radiation hydrodynamics code HYDRA [38,39]. HYDRA was set to use an Arbitrary Lagrangian Eulerian mesh that allows for mass advection, the quotidian equation of state (QEOS) [40], and conductivity from Lee and More [41]. The electron flux limiter was set to a value of 0.05. All opacities were computed assuming local thermodynamic equilibrium (LTE). The laser energy deposition mechanism at the relatively low irradiation intensities used in this experiment is assumed to be inverse bremsstrahlung absorption. Radiation transport was treated with multigroup radiation diffusion techniques and tabulated opacities. The temporal profile of the laser pulse was approximated by a 120 ps FWHM Gaussian function that closely mimics the experimental pulse.

Figure 5 shows simulated electron density maps for the times corresponding to the measured electron density distributions in Fig. 4. The simulations reproduce well the evolution of the plasma jet. The electron density at 2.6 ns is computed to reach 1.4×10^{20} cm^{-3} near the bottom of the target, in agreement with the measurements. Later in the evolution, side lobes are observed to form and separate in accordance with the experiment. The computed value of the peak electron density in the side lobes is similar to the measured value $[(1-1.3)\times10^{20}$ cm$^{-3}]$. The jet expansion velocity simulated by HYDRA is well matched with the experimental measurement, and the code predicts a maximum Mach number of $\sim$5. This good agreement between the HYDRA simulations and the experimental data was only achieved when taking into account radiation cooling of the plasma, as discussed later.

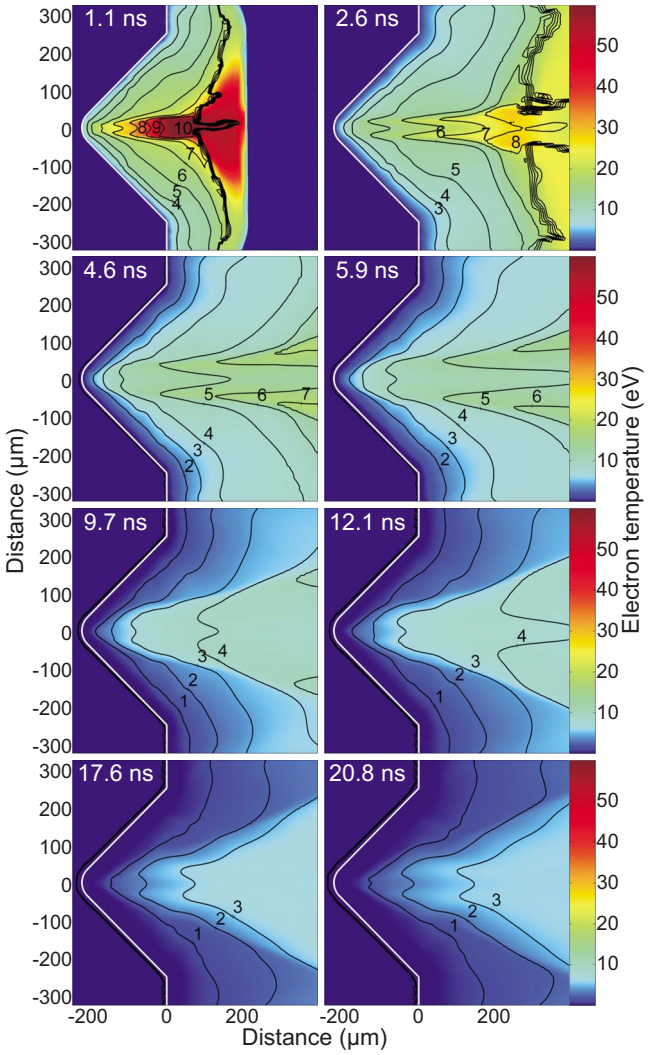

FIG. 6. (Color online) HYDRA simulated maps of the electron temperature T_e of the laser-created aluminum plasma. The black contour lines delimit regions of mean ionization Z_{mean} inside the plasma.

Figure 6 shows color maps of the computed electron temperature (T_e) with contours displaying the plasma mean degree of ionization (Z_{mean}). The simulations show that early in the evolution ($\sim$1 ns) the jet has a temperature of $T_e \sim 55$ eV and a high degree of ionization, $Z_{\text{mean}}=7-10$. The presence of $Z=10$ ions is confirmed by the time integrated soft x-ray spectrum presented in Fig. 7, that spans wavelengths from 3.5 to 6.5 nm. Several lines in Al X and Al XI, which can be efficiently excited with an electron distribution defined by an electron temperature of $\sim$50 eV, can be identified. Al XII transitions, whose excitation requires a significantly higher electron temperature, are not observed. These observations are consistent with the temperatures predicted by the code. The electron temperature maps also show that at times corresponding to more than 1 ns after the termination of the irradiation pulse, the plasma distributed along the walls of the target is cold ($T_e<15$ eV). At 2.6 ns the peak temperature drops to $\sim$25 eV, and is associated with plasma that has moved to a location outside the cavity. The plasma

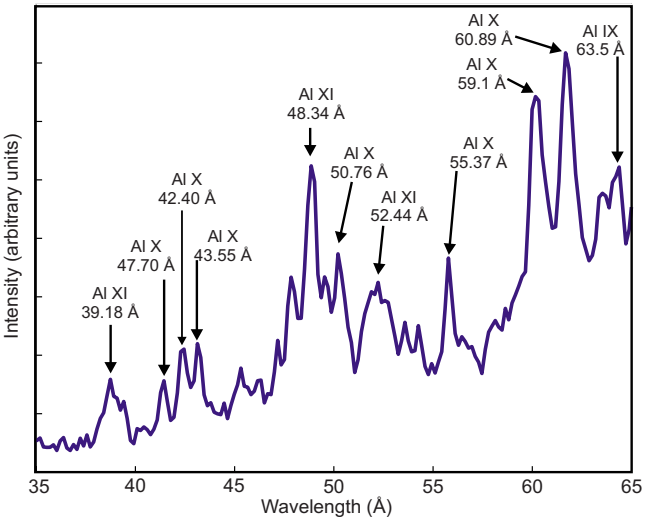

FIG. 7. (Color online) Time-integrated aluminum spectra in the region between 3.5 and 7.5 nm.

side lobes that appear later in time have low temperatures of less than 10 eV and low degree of ionization, $Z_{\text{mean}}<4$.

The computed pressure maps of Fig. 8 show that a high-pressure region forms at the bottom of the groove, resulting from the rapid convergence of plasma from the walls (see 300 ps frame). This localized high-pressure gradient acceler-

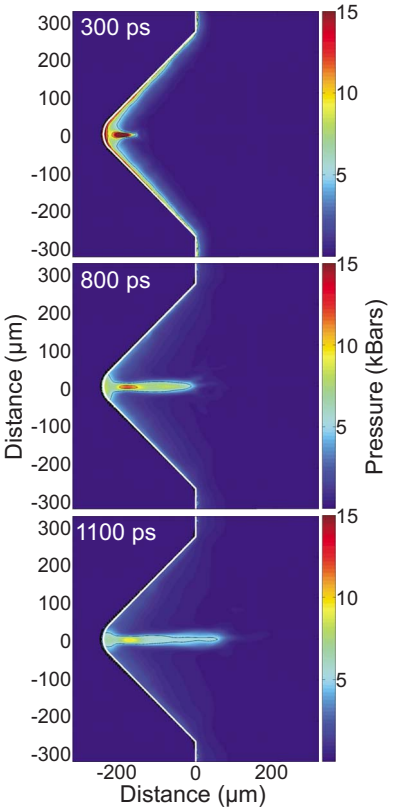

FIG. 8. (Color online) Computed plasma pressure distribution for different times measured with respect to the onset of the irradiation pulse. The large pressure gradients that develop at the bottom of the groove during the irradiation accelerate the plasma that initially forms the plasma jet.

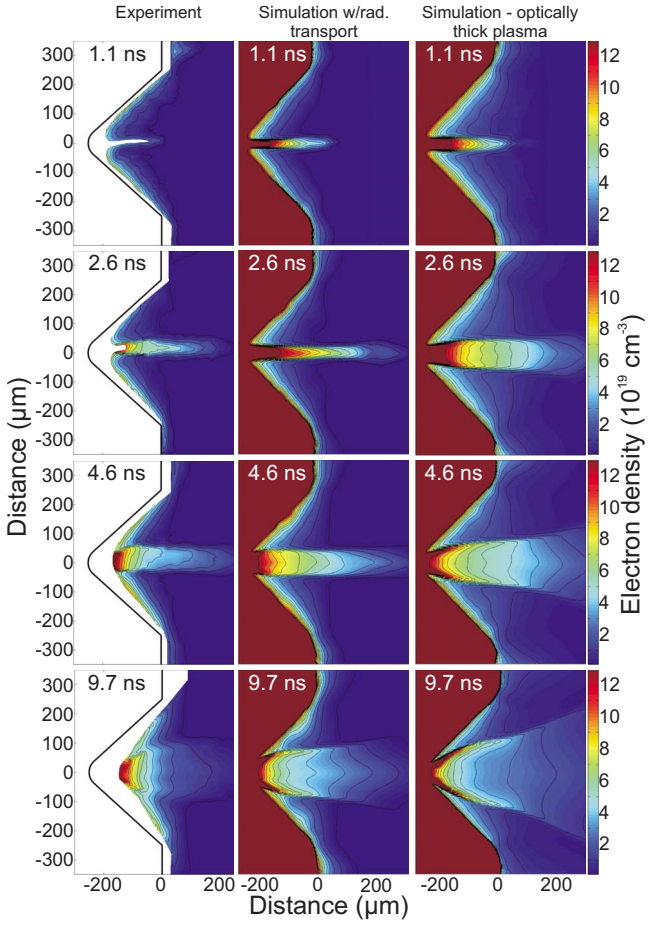

FIG. 9. (Color online) Comparison of Al plasma jet experimental data (left column) to HYDRA simulations with radiation transport (center column) and for an optically thick plasma (right column).

ates the ablated material outward at a Mach number of ~5. The interferograms show that at 1 ns this ablated material breaches the opening of the cavity as a plasma jet. At this time the highest pressures are located along the symmetry plane. These pressure gradients contribute to the progressive widening of the plasma plume.

Radiation cooling has been previously identified as an important mechanism in the collimation of plasma jets [15,17]. Figure 9 illustrates the effect of radiation cooling in our plasma jet. The measured electron density profiles are compared with the results of two different simulations. In the first, the plasma evolution was computed taking into account radiation transport, while in the second the plasma was assumed to be optically thick. In the former case, the radiation transport was computed using tabulated opacities generated using an average atom model at Lawrence Livermore National Laboratory. The comparison shows that radiation plays a significant role in the experimentally observed jet collimation. For the plasma conditions of our experiment, line radiation dominates radiation loss rates. Dielectric recombination and photorecombination are weaker by about two orders of magnitude and bremsstrahlung radiation is even less intense. In the simulated optically thick case, the plasma is computed to be significantly hotter (80 eV at 1.1 ns) than in the radiatively cooled plasma (55 eV at 1.1 ns), which translates into a higher plasma pressure on axis. The higher pressure in the optically thick case results in a broader, less collimated jet, and in the premature formation of the plasma side lobes, in disagreement with the experiment. The relative importance of radiation in aiding jet collimation is usually evaluated through the cooling parameter χ defined as the ratio of the radiation cooling time to the characteristic hydrodynamic time $\chi=\tau_{\mathrm{rad}}/\tau_{\mathrm{hydro}}$ [18]. The characteristic radiative cooling time is given by the total kinetic plasma energy content divided by the radiative flux q_{rad}: $\tau_{\mathrm{rad}}=[3k(T_E n_E+T_I n_I)]/2q_{\mathrm{rad}}$, and the characteristic hydrodynamic time $\tau_{\mathrm{hydro}}=R_{\mathrm{jet}}/v_{\mathrm{jet}}$ is the ratio of the jet width to the jet lateral expansion velocity. When $\chi<1$, the jet is strongly radiative and is classified as a radiatively cooled jet. The characteristic times were computed at different times during the plasma evolution using a spatial average of the plasma parameters within the jet calculated by HYDRA. During the first 2.5 ns of the evolution, $\tau_{\mathrm{rad}}\sim\tau_{\mathrm{hydro}}$, corresponding to a radiative cooling parameter of $\chi\sim1$. This classifies our jet as being in the coupled regime, where radiation cooling is comparable to adiabatic cooling. Simulations reveal that the role of radiation in cooling the jet decreases after the first 2.5 ns, when χ becomes increasingly larger than 1 and the jet is observed to undergo significant lateral expansion.

To better visualize the formation of the plasma jet and the subsequent development of the plasma side lobes, tracer particle trajectory plots were generated from the velocity vector fields computed by HYDRA at 10 ps intervals. Figure 10 shows the trajectory of initially equally spaced particles ablated at times of 30, 140, and 250 ps with respect to the beginning of the 120 ps FWHM laser heating pulse. Each frame follows the tracer particles from the time they leave the surface up to 5 ns in the evolution. Each alternating color shade indicates an elapsed time of 500 ps.

Figure 10 shows that mass ablated at different times during the laser heating pulse contributes differently to the formation of the jet. The frame corresponding to material ablated 30 ps after the initiation of the laser irradiation pulse reveals the successive arrival of plasma originating from the side walls to the symmetry plane. The trajectories are initially observed to be perpendicular to the target surface, as can be expected from the pressure gradients normal to the walls. The tracer particles with the highest velocities are those corresponding to the most intensely irradiated ~150-μm-wide central region of the target surface at the beginning of the laser pulse. These are the only tracer particles that reach the symmetry plane one nanosecond after the irradiation pulse. This is evidence that within the first nanosecond, the plasma jet only contains material ablated from the 150-μm-wide central region of the target. The 140 ps frame in Fig. 10 shows that the material ablated later during the irradiation pulse has a reduced velocity. This is in particular the case of plasma emanating from the central region of the groove, which is significantly slowed down by its encounter with downstream plasma created by mass ablated earlier during the irradiation pulse. This effect is even more evident in the 250 ps frame, corresponding to material ablated after the heating laser has deposited its energy, in which the mass ablated from the bottom of the groove is seen to expand only 70 μm along the symmetry plane within the first 5 ns.

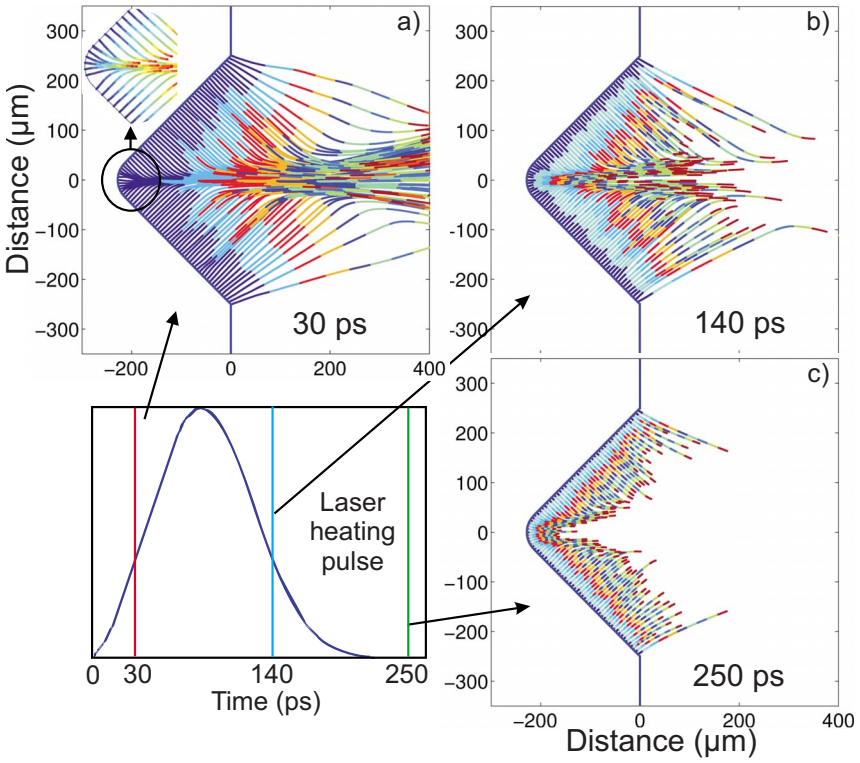

FIG. 10. (Color online) HYDRA simulations of particles trajectories leaving the target at different times during the laser heating pulse. The alternating colors represent 500 ps time steps and the complete trajectory spans 5 ns.

The role of the target tip in the formation of the plasma jet was investigated by comparing the results with simulations of a target with a 150-μm-wide opening at the bottom of the groove. It was found that without the vertex, a jetlike plasma structure still forms as a result of the collision of plasma arriving from the walls at the symmetry plane, but this jet has a reduced density and velocity. Just like in the case including the tip, the sequential arrival on axis of plasma generated at the target walls contributes to increase the mass of the jet. Later in the evolution the dominant pressure in the jet, which is not counterbalanced by the momentum of plasma ablated from the side walls, causes it to widen. The collision of the expanding plasma jet with the plasma generated at the walls forms the observed plasma side lobes.

Aside from the Mach number ($M \sim 5$) and cooling parameter ($\chi \sim 1$), the measurements and simulations allow the computation of other dimensionless parameters for comparison with other jets [18]. The ratio of jet density to ambient medium (the latter taken here as the density of the plasma surrounding the jet) is $\eta = \rho_{\mathrm{jet}}/\rho_{\mathrm{amb}} > 10^2$. The Reynolds number $R_e = R_{\mathrm{jet}} v_{\mathrm{jet}}/\upsilon \sim 4 \times 10^5$ and Peclet number $P_e = R_{\mathrm{jet}} v_{\mathrm{jet}}/\kappa \sim 10$ were computed at 1.1 ns using Spitzer's kinematic viscosity υ, and kinematic thermal diffusivity κ, and values of $n_e \sim 8 \times 10^{19}$ cm^{-3}, $T_e \sim 40$ eV resulting from averaging these quantities within the jet. This means that both viscous drag and thermal conduction can be neglected compared with inertial forces and the advection of kinetic energy. The ion-ion collision mean free path is computed to be $\lambda_{\mathrm{mfp}} < 1$ μm, significantly shorter than the plasma lateral dimension, R_{jet}, resulting in a localization parameter $\delta = \lambda_{\mathrm{mfp}}/R_{\mathrm{jet}} < 10^{-2}$ corresponding to a highly collisional plasma. This high degree of collisionality allows the plasma to be simulated with a hydrodynamic code.

V. CONCLUSIONS

The evolution of a dense ($n_e \sim 10^{20}$ cm^{-3}) collisional plasma jet created by laser irradiation of triangular aluminum grooves at intensities of $\sim 1 \times 10^{12}$ W cm^{-2} with 120 ps duration laser pulses was studied using soft x-ray laser interferometry. The highly collisional nature of this jet allows it to be modeled with a hydrodynamic code. The jet initially expands at a velocity of $\sim 3 \times 10^7$ cm s^{-1} with a Mach number of ~ 5 and reaches the edge of the 250-μm-deep groove within the first nanosecond after laser irradiation. The jet is initiated by ablated material accelerated by a large pressure gradient at the target tip, and is augmented by the continual sequential arrival of wall material along the symmetry plane, where it collides and is redirected outward. Early in the evolution, the jet has an electron temperature of ~ 55 eV and is highly ionized, radiating strongly from Al X and Al XI ion lines. Simulations reveal that radiation cooling plays a significant role in reducing the pressure and maintaining the collimation of the jet. During the first few nanoseconds, when the jet possesses a high length-to-width ratio of ~ 10, the jet is in the radiatively coupled regime ($\chi \sim 1$). Radiation cooling then decreases as time evolves. Later in the evolution, the collision of the widening plasma jet with the counter propagating plasma generated at the walls forms plasma side lobes.

These results demonstrate that well collimated plasma jets with parameters in a range of significant interest can be generated with low-energy laser pulses, opening the possibility of studying phenomena such as the interaction of plasma jets with other plasmas in a small laboratory setting. The measurements also show that soft x-ray laser interferometry is a

powerful tool for the study of dense plasmas dynamics and the validation of hydrodynamic codes. The results can motivate further work using soft x-ray interferometry to study scaled astrophysical phenomena in the laboratory.

ACKNOWLEDGMENTS

The authors would like to thank Marty Marinak for his helpful discussions regarding the code HYDRA. This research was sponsored by the National Nuclear Security Administration under the Stewardship Science Academic Alliances program through U.S. Department of Energy Research Grant No. DE-FG52-06NA26152, using facilities from the NSF ERC Center for Extreme Ultraviolet Science and Technology, award EEC-0310717. Part of this work was performed under the auspices of the U.S. Department of Energy by Lawrence Livermore National Laboratory under Contract No. DE-AC52-07NA27344.

[1] A. H. Bride and R. A. Perley, Annu. Rev. Astron. Astrophys. **22**, 319 (1984).
[2] H. Zinnecker, M. J. McCaughrean, and J. T. Rayner, Nature **394**, 862 (1998).
[3] P. M. Bellan, Phys. Plasmas **12**, 058301 (2005).
[4] K. J. Borkowski, J. M. Blondin, and J. P. Harrigton, Astrophys. J. Lett. **482**, L97 (1997).
[5] J. M. Blondin, B. A. Fryxell, and A. Konigl, Astrophys. J. **360**, 370 (1990).
[6] M. L. Norman, L. Smarr, K.-H. A. Winkler, and M. D. Smith, Astron. Astrophys. **113**, 285 (1982).
[7] J. M. Foster, B. H. Wilde, P. A. Rosen, T. S. Perry, M. Fell, M. J. Edwards, B. F. Lasinski, R. E. Turner, and M. L. Gittings, Phys. Plasmas **9**, 2251 (2002).
[8] Ph. Nicolai, V. T. Tikhonchuk, A. Kasperczuk, T. Pisarczyk, S. Borodziuk, K. Rohlena, and J. Ullschmied, Phys. Plasmas **13**, 062701 (2006).
[9] A. Kasperczuk, T. Pisarczyk, S. Borodziuk, J. Ullschmied, E. Krousky, K. Masek, M. Pfeifr, K. Rohlena, J. Skala, and H. Hora, Phys. Plasmas **13**, 062704 (2006).
[10] A. Kasperczuk, T. Pisarczyk, S. Borodziuk, J. Ullschmied, E. Krousky, K. Masek, M. Pfeifr, K. Rohlena, J. Skala, and P. Pisarczyk, Phys. Plasmas **14**, 032701 (2007).
[11] S. R. Goldman, S. E. Caldwell, M. D. Wilke, D. C. Wilson, C. W. Barnes, W. W. Hsing, N. D. Delamater, G. T. Schappert, J. W. Grove, E. L. Lindman, J. M. Wallace, R. P. Weaver, A. M. Dunne, M. J. Edwards, P. Graham, and B. R. Thomas, Phys. Plasmas **6**, 3327 (1999).
[12] S. R. Goldman, C. W. Barnes, S. E. Caldwell, D. C. Wilson, S. H. Batha, J. W. Grove, M. L. Gittings, W. W. Hsing, R. J. Kares, K. A. Klare, G. A. Kyrala, R. W. Margevicius, R. P. Weaver, M. D. Wilke, A. M. Dunne, M. J. Edwards, P. Graham, and B. R. Thomas, Phys. Plasmas **7**, 2007 (2000).
[13] S. S. Harilal, C. V. Bindhu, and H.-J. Kunze, J. Appl. Phys. **89**, 4737 (2001).
[14] S. V. Lebedev, J. P. Chittenden, F. N. Beg, S. N. Bland, A. Ciardi, D. Ampleford, S. Hughes, M. G. Haines, A. Frank, E. G. Blackman, and T. Gardiner, Astrophys. J. **564**, 113 (2002).
[15] D. R. Farley, K. G. Estabrook, S. G. Glendinning, S. H. Glenzer, B. A. Remington, K. Shigemori, J. M. Stone, R. J. Walace, G. B. Zimmerman, and J. A. Harte, Phys. Rev. Lett. **83**, 1982 (1999).
[16] K. Shigemori, T. Dittmire, B. A. Remington, V. Yanovsky, D. Ryutov, K. G. Estabrook, M. J. Edwards, A. J. MacKinnon, A. M. Rubenchik, K. A. Keilty, and E. Liang, Astrophys. J. Lett. **533**, L159 (2000).
[17] K. Shigemori, R. Kodama, D. R. Farley, T. Koase, K. G. Estabrook, B. A. Remington, D. D. Ryutov, Y. Ochi, H. Azechi, J. Stone, and N. Turner, Phys. Rev. E **62**, 8838 (2000).
[18] D. Ryutov, R. P. Drake, J. Kane, E. Liang, B. A. Remington, and W. M. Wood-Vasey, Astrophys. J. **518**, 821 (1999).
[19] S. V. Lebedev, J. P. Chittenden, F. N. Beg, S. N. Bland, A. Ciardi, D. Ampleford, S. Hughes, M. G. Haines, A. Frank, E. G. Blackman, and T. Gardiner, Astrophys. J. **564**, 113 (2002).
[20] V. A. Gribkov, O. N. Krokhin, V. Ya Nikulin, O. G. Semenov, and G. V. Sklizkov, Sov. J. Quantum Electron. **5**, 530 (1975).
[21] D. T. Attwood, D. W. Sweeney, J. M. Auerbach, and P. H. Y. Lee, Phys. Rev. Lett. **40**, 184 (1978).
[22] L. B. Da Silva, T. W. Barbee, Jr., R. Cauble, P. Celliers, D. Ciarlo, S. Libby, R. A. London, D. Matthews, S. Mrowka, J. C. Moreno, D. Ress, J. E. Trebes, A. S. Wan, and F. Weber, Phys. Rev. Lett. **74**, 3991 (1995).
[23] A. S. Wan, T. W. Barbee, Jr., R. Cauble, P. Celliers, L. B. Da Silva, J. C. Moreno, P. W. Rambo, G. F. Stone, J. E. Trebes, and F. Weber, Phys. Rev. E **55**, 6293 (1997).
[24] A. S. Wan, T. W. Barbee, Jr., R. Cauble, P. Celliers, L. B. Da Silva, J. C. Moreno, P. W. Rambo, G. F. Stone, J. E. Trebes, and F. Weber, IEEE Trans. Plasma Sci. **27**, 120 (1999).
[25] H. Tang, O. Guilbaud, G. Jamelot, D. Ros, A. Klisnick, D. Joyeux, D. Phalippou, M. Kado, M. Nishikino, M. Kishimoto, K. Sukegawa, M. Ishino, K. Magashima, and H. Daido, Appl. Phys. B: Lasers Opt. **78**, 975 (2004).
[26] J. Filevich, K. Kanizay, M. C. Marconi, J. L. A. Chilla, and J. J. Rocca, Opt. Lett. **25**, 356 (2000).
[27] J. Filevich, J. J. Rocca, M. C. Marconi, R. F. Smith, J. Dunn, R. Keenan, J. R. Hunter, S. J. Moon, J. Nilsen, A. Ng, and V. N. Shlyaptsev, Appl. Opt. **43**, 3938 (2004).
[28] J. J. Rocca, C. H. Moreno, M. C. Marconi, and K. Kanizay, Opt. Lett. **24**, 420 (1999).
[29] J. J. Rocca, E. C. ammarsten, E. Jankowska, J. Filevich, M. C. Marconi, S. Moon, and V. N. Shlyaptsev, Phys. Plasmas **10**, 2031 (2003).
[30] M. Purvis, J. Grava, J. Filevich, M. C. Marconi, J. Dunn, S. J. Moon, V. N. Shlyaptsev, E. Jankowska, and J. J. Rocca, Phys. Rev. E **76**, 046402 (2007).
[31] R. Kodama, K. A. Tanaka, Y. Sentoku, T. Matsushita, K. Takahashi, HJ. Fujita, Y. Kitagawa, Y. Kato, T. Yamanaka, and K. Mima, Phys. Rev. Lett. **84**, 674 (2000).
[32] R. F. Smith, J. Dunn, J. Nilsen, V. N. Shlyaptsev, S. Moon, J. Filevich, J. J. Rocca, M. C. Marconi, J. R. Hunter, and T. W. Barbee, Jr., Phys. Rev. Lett. **89**, 065004 (2002).
[33] B. R. Benware, C. D. Macchietto, C. H. Moreno, and J. J.

Rocca, Phys. Rev. Lett. **81**, 5804 (1998).
[34] Y. Liu, M. Seminario, F. G. Tomasel, C. Chang, C. H. Moreno, J. J. Rocca, and D. T. Attwood, Phys. Rev. A **63**, 033802 (2001).
[35] Yu. A. Uspenskii, V. E. Levashov, A. V. Vinogradov, A. I. Fedorenko, V. V. Konsratenko, Tu. P. Pershin, E. N. Zubarev, and V. Yu. Fedotov, Opt. Lett. **23**, 771 (1998).
[36] T. Kita, T. Harada, N. Nakano, and H. Kuroda, Appl. Opt. **22**, 512 (1983).
[37] J. Filevich, J. J. Rocca, M. C. Marconi, S. J. Moon, J. Nilsen, J. H. Scofield, J. Dunn, R. F. Smith, R. Keenan, J. R. Hunter, and V. N. Shlyaptsev, Phys. Rev. Lett. **94**, 035005 (2005).
[38] M. M. Marinak, S. W. Hann, T. R. Dittrich, R. E. Tipton, and G. B. Zimmerman, Phys. Plasmas **5**, 1125 (1998).
[39] M. M. Marinak, G. D. Kerbel, N. A. Gentile, O. Jones, D. Munro, S. Pollaine, T. R. Dittrich, and S. W. Haan, Phys. Plasmas **8**, 2275 (2001).
[40] R. M. More, K. H. Warren, D. A. Young, and G. B. Zimmerman, Phys. Fluids **31**, 3059 (1988).
[41] Y. T. Lee, and R. M. More, Phys. Fluids **27**, 1273 (1984).